Magnetization reversal and local switching fields of ferromagnetic Co/Pd microtubes with radial magnetization

Norbert Puwenberg,[1,2] Christopher F. Reiche,[3] Robert Streubel,[4] Mishal Khan,[1,2] Dipankar Mukherjee,[1,2]
Ivan V. Soldatov,[1] Michael Melzer,[1] Oliver G. Schmidt,[1,5] Bernd Büchner,[1,2] and Thomas Mühl[1]

[1]*Leibniz Institute for Solid State and Materials Research IFW Dresden, 01069 Dresden, Germany*
[2]*Institute of Solid State and Materials Physics, Technische Universität Dresden, 01069 Dresden, Germany*
[3]*Department of Electrical and Computer Engineering, University of Utah, Salt Lake City, Utah 84112, USA*
[4]*Materials Sciences Division, Lawrence Berkeley National Laboratory, Berkeley, California 94720, USA*
[5]*Material Systems for Nanoelectronics, Technische Universität Chemnitz, 09107 Chemnitz, Germany*

Three-dimensional nanomagnetism is a rapidly growing field of research covering both noncollinear spin textures and curved magnetic geometries including microtubular structures. We spatially resolve the field-induced magnetization reversal of free-standing ferromagnetic microtubes utilizing multifrequency magnetic force microscopy (MFM). The microtubes are composed of Co/Pd multilayer films with perpendicular magnetic anisotropy that translates to an anisotropy with radial easy axis upon rolling-up. Simultaneously mapping the topography and the perpendicular magnetostatic force derivative, the relation between surface angle and local magnetization configuration is evaluated for a large number of locations with slopes exceeding 45 degrees. The angle-dependence of the switching field is concurrent with the Kondorsky model, i.e., the rolled-up nanomembrane behaves like a planar magnetic film with perpendicular anisotropy and a pinning dominated magnetization reversal. Additionally, we discuss methodological challenges when detecting magnetostatic force derivatives near steep surfaces.

I. INTRODUCTION

Recent advances in synthesis science, theory, and instrumentation combined with novel electronics concepts have boosted the research interest into three-dimensional (3D) nanomagnetism [1] covering both noncollinear spin textures and curved magnetic geometries [2,3]. The expansion into the third dimension does not only allow for vertically stacking microelectronics (2.5-dimensional architectures), but also launches new functionalities associated with curvature and shape. The effect of curvature and shape can be classified into three categories: (i) curvature-induced vector spin exchange [4] and magnetochiral effects [5]; (ii) topology-driven modifications; and (iii) spin frustration and pinning in 3D networks. These mechanisms are the foundation for revolutionary concepts, including tubular magnonic waveguides with an unidirectional, reconfigurable dispersion relation [6], azimuthally magnetized tubes with small magnetic anisotropy for giant magnetoimpedance-based magnetoencephalography [7], tubular channels for fuel-free transport of superparamagnetic beads [8], and domain wall propagation in 3D racetrack memories [9]. The common theme of 3D nanomagnetism is the governance of magnetic properties under the 3D distribution of the magnetization configuration. Hence a profound understanding of underlying mechanisms and the optimization of device performance demand the visualization of magnetization configuration. Addressing the transformative challenge of imaging the magnetic vector field, numerous techniques have been developed and advanced, including high-resolution Lorentz microscopy [10], vector field electron tomography [11,12], and magnetic x-ray microscopy and tomography [13,14]. In addition to these expensive tools operated at large-scale user facilities, cost-efficient table-top setups have been explored based on magneto-optical Kerr effect magnetometry [15] and, as outlined in this work, multifrequency magnetic force microscopy.

Here we study free-standing Co/Pd microtubes composed of rolled-up multilayers. Co/Pd multilayers are sandwich-structured magnetic thin films whose magnetic anisotropy, i.e., strength, type, and direction of a potential perpendicular magnetic easy axis, can be tailored via tuning the thickness of individual cobalt and palladium layers [16–18]. Our Co/Pd microtube samples are manufactured by means of strain-engineering of magnetic multilayer films with tube diameters in the micrometer range. The perpendicular magnetic anisotropy of the initially planar Co/Pd film translates to an anisotropy with radial easy axis upon forming a rolled-up nanomembrane [13]. The appeal of these 3D ferromagnetic nanostructures ranges from prototypical systems for magnetic x-ray tomography [13] to experimental demonstration of theoretically predicted phenomena as already described above. It was already demonstrated that magnetic force microscopy (MFM) is suitable to map the magnetic stray-field of free-standing microtubes with radial magnetization [19]. In the present study, we investigate the field-dependent magnetization processes of a radially magnetized Co/Pd microtube at the nanoscale facilitating multifrequency MFM, and determine the model describing the reversal processes. Multifrequency MFM is a dedicated MFM technique employing two

094438-1

superimposed flexural oscillation modes of the cantilever to simultaneously map the topography of the tubular surface and its magnetic stray-field landscape with high sensitivity and high spatial resolution. This special MFM technique was inspired by the work of Schwenk *et al.* [20] and offers the advantage of robust topography tracking of steep surfaces without crosstalk from magnetostatic interactions combined with simultaneous mapping of the magnetic signal in a true noncontact single pass procedure. However, applying MFM to highly nonhorizontal surfaces opens up conceptual limitations that are known from in-plane or pendulum-type MFM [21,22]. In particular, a MFM tip oscillating parallel to a local surface and along a domain wall does not provide a MFM signal. The MFM insensitivity in this particular case can, in future, be bypassed by harnessing the recently introduced bidirectional mode of MFM operation [23,24].

II. MAGNETIZATION REVERSAL

The magnetic field-driven magnetization reversal in real systems with uniaxial anisotropy can generally be approximated by either of three analytical models, revealing the underlying mechanism: (i) Stoner-Wohlfarth model based on the coherent rotation of magnetic moments in very small particles [25,26]; incoherent modes, such as curling- or buckling-type reversal in ferromagnetic nanowires [27–30]; and Kondorsky model referring to a pinning dominated reversal [31,32]. Figure 1 shows a comparison between a coherent rotation (Stoner-Wohlfarth model) and a pinning dominated reversal (Kondorsky model) in ferromagnetic samples.

The magnetic switching field H_S depends on the angle ϕ between external magnetic field H and easy axis of the magnetization. According to the Stoner-Wohlfarth model, $H_S(\phi) = H_S(0°) \cdot (\cos^{2/3}\phi + \sin^{2/3}\phi)^{-3/2}$ describes the switching of single domain particles with sizes of the order of 10–100 nm [33,34].

In general, larger-scaled ferromagnetic solids like thin films possess a multidomain (MD) structure, in which the magnetic domains are separated by domain walls whose size is defin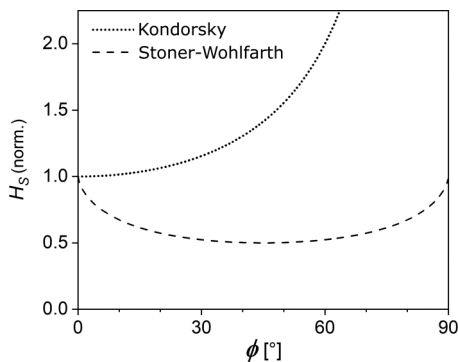ed by the interplay of exchange interaction and magnetic anisotropy energy [35]. A transition from a single-domain state to a state split up into multiple domains reduces magnetostatic stray-field contributions and thus lowers the magnetostatic energy of the ferromagnet. The domain walls play an important role in the magnetization reversal in MD materials since magnetic switching processes involve nucleation of domains with reversed magnetization and a displacement of domain walls in the material, which can be hindered by magnetic inhomogeneities [36,37]. Even when the external magnetic field is insufficient to reverse the magnetization through a coherent rotation of the magnetic moments in the material, the component of the applied magnetic field parallel to the easy axis of magnetization can push the domain wall through the ferromagnetic solid [37]. This results in a Kondorsky-type behavior of the switching field $H_S(\phi) = H_S(0°) \cdot 1/\cos\phi$, which was observed, for example, in Co/Pt thin films and in Sr/Fe films possessing a large density of pinning sites [34,37].

III. EXPERIMENTAL TECHNIQUES AND DATA EVALUATION

A. Multifrequency magnetic force microscopy

MFM in frequency-modulation mode takes advantage of the frequency shift Δf of a cantilever resonance as a direct measurement signal, which reflects the interaction between tip and sample [38]. A tip oscillating in the z-direction is sensitive to the derivative of the tip-sample force z-component with respect to the normal spatial z-coordinate ($\partial F_z/\partial z$). Modeling the MFM tip as a perfect point dipole with a magnetic moment m_z along the z-axis, the relation between frequency shift and the z-component of the magnetostatic stray-field H_z emerging from a magnetically active sample can be expressed by [39]

$$\Delta f = -\mu_0 \, m_z \, \frac{f_0}{2k} \, \frac{\partial^2 H_z}{\partial z^2} \, . \tag{1}$$

Here f_0 denotes the resonance frequency of the cantilever and k its flexural stiffness. In MFM, the separation of magnetostatic contrast and sample topography is challenging and often realized by using dual-passage methods in air, in which each scan line is scanned twice. The first pass in intermittent tip-sample contact maps the topography, the second pass at an increased tip-sample distance provides sensitivity to magnetostatic tip-sample interactions [40,41].

The approach we use for microtube imaging employs multiple cantilever excitation frequencies and is capable to decouple magnetostatic interactions from the sample topography even for large height variations up to several micrometers and slopes well above 45°. In contrast to the aforementioned two-pass technique, the fundamental and second mode flexural cantilever oscillation serve as independent measurement channels that record magnetostatic and topographic information simultaneously in a single pass [20]. In our case, the amplitude of the second oscillation mode is used to control the tip-sample distance. The second mode oscillation is excited by applying an AC voltage $\hat{U}_{AC}$ between MFM tip and sample at half the frequency of the second cantilever eigenmode $f_{AC} = 1/2 \cdot f_2$. The tip-sample arrangement forms a capacitor with capacitance C_{ts}. The emergent electrostatic force component

FIG. 1. Simulated switching curves for Kondorsky [$H_S(\phi) = H_S(0°) \cdot 1/\cos\phi$] and Stoner-Wohlfarth [$H_S(\phi) = H_S(0°) \cdot (\cos^{2/3}\phi + \sin^{2/3}\phi)^{-3/2}$] type magnetization reversal. H_S is the switching field normalized to the switching field at 0°, at which $H_S(0°) = 1$ applies, and ϕ denotes the angle between the applied field and the easy axis of magnetization.

$F_{2f_{AC}}$ becomes [20]

$$F_{2f_{AC}}(z) = -\frac{1}{4}\frac{\partial C_{ts}(z)}{\partial z}\hat{U}_{AC}^2 \cos(2 \cdot 2\pi f_{AC} t) . \qquad (2)$$

Both periodic force $F_{2f_{AC}}$ and second-mode oscillation amplitude A_2 strongly depend on the tip-sample distance z_{ts} due to the $\partial C_{ts}/\partial z$ distance dependence. Thus A_2 allows for controlling the tip-sample distance keeping the amplitude constant via a distance control feedback loop. The control of the tip-sample distance therefore corresponds to a rough tracking of the sample surface. A phase-locked loop (PLL) ensures that the second mode is excited at its resonance. This measure prevents crosstalk between force gradients, produced by magnetostatic interactions or contact potential differences, and the second-mode amplitude, and therefore on the distance control. Note that the amplitude-distance relation depends on the Q-factor of the driven oscillation, which in turn is affected by local changes of dissipative magnetization processes, potentially corrupting the distance control [20]. However, in our case, we did not observe a location dependence of the dissipation in the fundamental oscillation mode. Hence guaranteeing a constant tip-sample distance by the second-mode cantilever oscillation, the frequency shift of the mechanically excited fundamental mode Δf_1 can be used to map force gradients originating from the sample magnetostatic stray-field distribution. To ensure well-defined imaging conditions, the amplitude A_1 of the fundamental mode oscillation is kept constant by a PI controlled feedback loop. The result is a superposition of two oscillations at the corresponding resonance frequencies of fundamental and second cantilever mode with amplitudes maintained at a constant level. Multifrequency MFM mode can be, in principle, implemented in any commercially available magnetic force microscope by using an additional lock-in amplifier. However, the microscope controller must allow for accessing the detector signal and the tip-sample bias input. Moreover, a free auxiliary input needs to be available to feed-in the amplitude signal A_2 from the external lock-in amplifier. A_2 can then serve as input for the internal tip-sample distance control of the microscope scanner.

B. Microtube preparation and MFM experiments

A ferromagnetic $[\text{Co}(0.4\,\text{nm})/\text{Pd}(0.7\,\text{nm})]_5$ multilayer stack with perpendicular anisotropy, fully saturated remanent state, and capped with 2-nm Pd forms the magnetic foundation of the investigated microtubes [13]. This magnetic multilayer film was subsequently sputter-deposited with a strained polycrystalline titanium layer with a thickness of 20 nm onto a lithographically patterned sacrificial photoresist layer [42]. The patterns consist of $20 \times 20\,\mu$m squares with a period of $50\,\mu$m. Upon selectively resolving the sacrificial layer, the normal strain gradient in the titanium film caused an upward bending and rolling up of the complete layer system into a tubular geometry with a radial magnetic easy axis. Suitable microtubes were identified and characterized with scanning electron microscopy (SEM) and located in the MFM using external CCD cameras. The microtube discussed below is shown in Fig. 2(a).
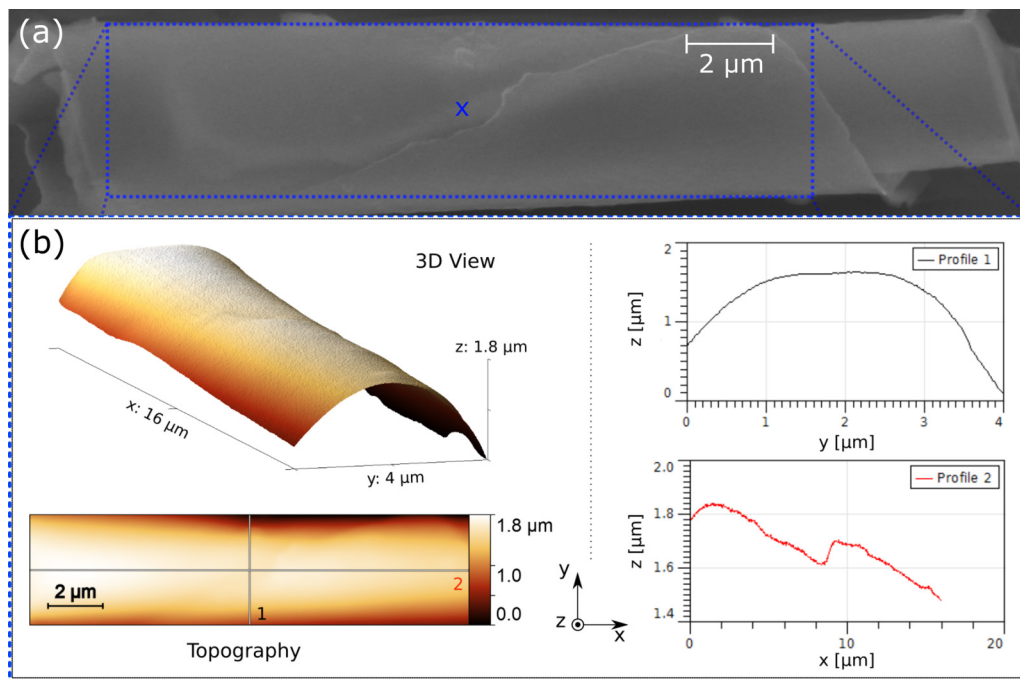

FIG. 2. (a) SEM image of a Co/Pd microtube with two windings: Frame with center point "x" shows the range of the MFM scan, representing an area of $16\,\mu$m x $4\,\mu$m. (b) MFM topographic channel, recorded in zero-field from top left to bottom right at a tip-surface distance of (205 ± 10) nm, with the latter measured above the center point. In this experiment, $A_2 = 0.22$ nm, if $\hat{U}_{AC} = 1.0$ V is applied between MFM tip and sample. Shown are 3D and top view topographic images with two line profiles across the tube circumference (profile 1) and along the tube axis (profile 2). Profile 2: A step in the tube topography is visible which originates from the edge of the outer winding that is wrapped around the inner winding with a spacing of approximately 100 nm.
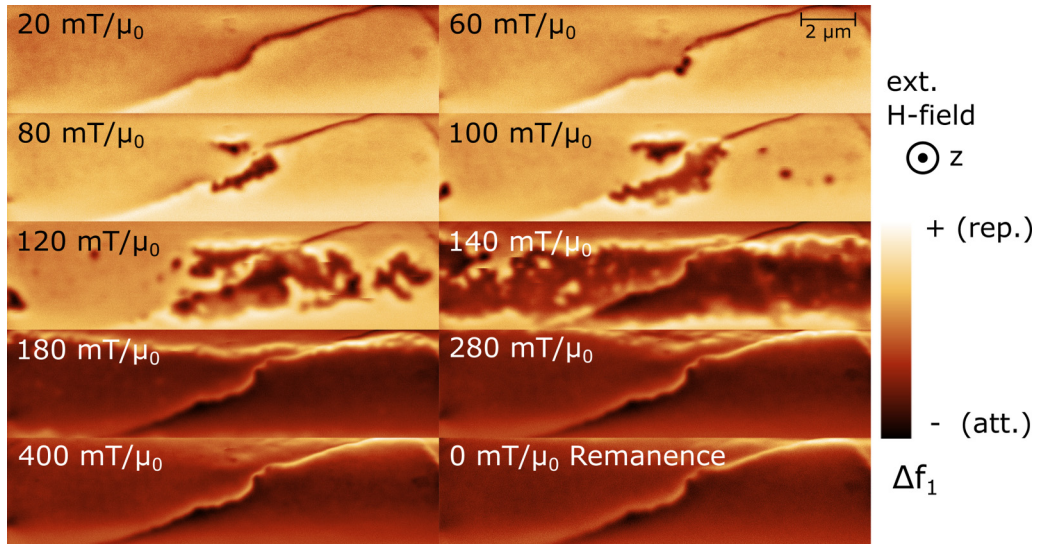
FIG. 3. Fundamental mode frequency shift (Δf_1) maps showing the magnetostatic interaction (repulsive/attractive) between MFM tip and microtube surface for different values of the applied magnetic field. A tip-surface distance of (205 ± 10) nm and a constant amplitude $A_1 = 10$ nm were used. The direction of the applied field is perpendicular to the image plane and points toward the reader. The tip magnetization is, in first approximation, oriented in the direction of the applied field. Dark (bright) contrast corresponds to attractive (repulsive) interaction. The magnetostatic contrast near the overlapping edge is expected in the case of stray fields near edges of perpendicularly magnetized thin films.

We use a NanoScan AG hr-MFM device supplemented by a Zurich Instruments HF2LI lock-in amplifier, and commercial cone-shaped Team Nanotec HR-MFM45 ML3 tips with a hard magnetic cobalt alloy coating and a nominal cantilever stiffness of 0.7 N/m. The resonance frequencies for fundamental and second-mode flexural cantilever oscillation were determined sweeping the excitation frequency and locating the resonance peaks in the amplitude spectrum. To reveal the position of the select microtube for subsequent magnetic imaging, large area overview maps of the fundamental mode frequency shift were performed. For this purpose a high DC bias voltage of 3 V was applied between tip and sample leading to a strong electrostatic field gradient, which dominates the frequency shift even for tip-sample distances $>6 \mu$m. A PLL-controlled AC voltage with a frequency f_{AC} equal to half the second flexural eigenmode of the cantilever and a peak amplitude of $\hat{U}_{AC} = 1.0$ V was applied between tip and sample. We minimized the electrostatic contrast in MFM images by compensating the contact potential between tip and sample surface via an additional DC tip-sample bias voltage. After aligning the scan area to cover the major part of the microtube surface, the center point of the MFM scan area is used to determine the contact potential difference by sweeping the DC bias at a fixed tip-sample distance of (205 ± 10) nm, see Fig. 2(b).

Prior to MFM measurements, the microtube was saturated in an external magnetic field perpendicular to the image plane at $-430 \frac{mT}{\mu_0}$. The field was provided by a calibrated perpendicular field device based on a cylinder-shaped NdFeB permanent magnet. For field-dependent measurements, the field direction was rotated by 180° to enable fields with opposite polarity. In-field measurements were performed at incremental steps up to a final field of $400 \frac{mT}{\mu_0}$. The remanent state was recorded after reaching a maximum field of $430 \frac{mT}{\mu_0}$.

Figure 3 shows a selection of several frequency shift maps that form the basis for a detailed evaluation of the local magnetization reversal process in the microtube.

At $60 \frac{mT}{\mu_0}$, the first reversed domain emerges, whose magnetization is aligned along the applied field direction. As the magnetization of this domain and the tip magnetization are oriented almost parallel to each other, the detected attractive magnetostatic interaction between them leads to a negative frequency shift Δf_1 in the local MFM response. The location of the first reversed domain is characterized by two features: It appears at the edge of the outer winding and the local surface normal is nearly parallel to the external field. At larger perpendicular fields between $100 \frac{mT}{\mu_0}$ and $120 \frac{mT}{\mu_0}$, more domains form predominantly in regions with the surface normal being parallel to the external field, while existent attractive domains expand primarily along the tube axis. At $280 \frac{mT}{\mu_0}$, the magnetization reversal is nearly complete, except for some regions at the upper edge of the scanning range, which represent locations with large angles between external field and surface normal. The MFM maps at $400 \frac{mT}{\mu_0}$ and at the subsequent remanent state, after increasing the field to a maximum value of $430 \frac{mT}{\mu_0}$, look similar despite different anticipated magnetization configurations. Here we assume a locally homogenous radial magnetization in the investigated microtube area at remanence, and a tilt of the magnetization toward the external magnetic field at $400 \frac{mT}{\mu_0}$.

The experimental results obtained from the rolled-up films were further compared to their planar counterparts to identify effects induced by rolling, e.g., three-dimensional (3D) shape. The reversal of the planar, nonrolled-up film was studied by polar magneto-optical Kerr effect (MOKE) magnetometry [43] in a magnetic field up to $1 \frac{T}{\mu_0}$ aligned perpendicular to the film plane. The MOKE signal was detected in a wide-field
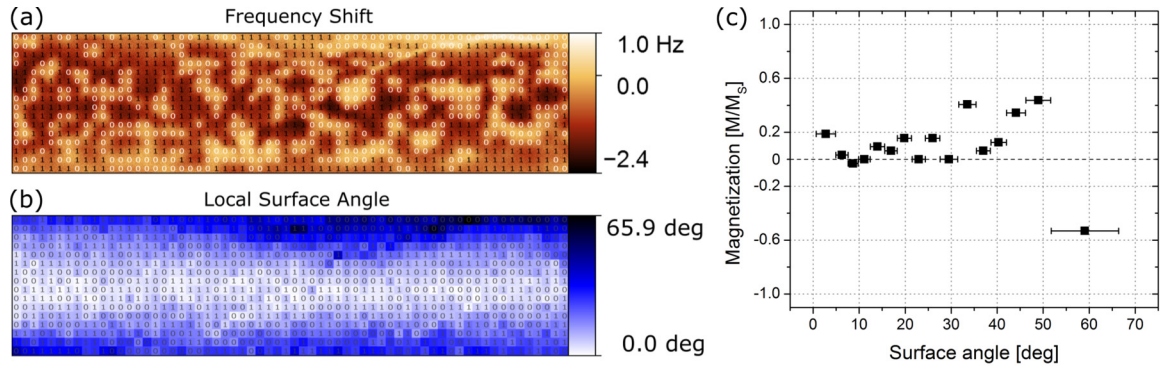
FIG. 4. (a) MFM frequency shift of the demagnetized state and (b) surface angle map of the same microtube region as shown in Figs. 2 and 3. The numbers "0" and "1" shown in (a) and (b) refer to predominantly repulsive and attractive magnetostatic interactions, respectively. (c) Angle-dependent normalized net magnetization: Every single data point corresponds to one specific angle interval, each containing 64 cells. The bars indicate the boundaries of the angle intervals. The net magnetization scatters around zero for most data points, i.e., $N_a \approx N_r$. For large angles above $46°$ the net magnetization fluctuates heavily around zero.

magneto-optical Kerr microscope that was equipped with a motorized analyzer to compensate the polar Faraday effect in the objective lens [44]. MOKE hysteresis loops were obtained by integrating the Kerr intensity in a selectable image area, and along the loop the domains were recorded simultaneously (not shown in the paper).

C. Statistical evaluation of magnetization status

For further quantitative analysis, the magnetization reversal process is statistically evaluated as a function of the surface orientation with respect to the external magnetic field. The procedure is first demonstrated on the example of the demagnetized state, set after decreasing an AC magnetic field applied perpendicularly to the sample substrate [Fig. 4(a)].

Taking advantage of the perpendicular magnetic anisotropy of the magnetic film, the MFM frequency shift map [Fig. 4(a)] can be translated to a radial magnetization configuration with bright and dark regions pointing inward and outward, respectively. To facilitate the evaluation of the local magnetization state, a matrix consisting of 64×16 cells was created using the original 1024×256 px data and placed on top of the MFM map. The switching status of each cell was determined with an ad hoc ansatz: Cells with dominating bright and dark contrast were manually assigned to the magnetization status "0" (repulsive) and "1" (attractive), referring to a magnetization pointing inward and outward, respectively. According to Li *et al.* [45] a statistic estimate of the normalized net magnetization M/M_S of the sample region covered by the matrix or by specific parts of the matrix can be calculated as

$$\frac{M}{M_s} = \frac{N_a - N_r}{N_a + N_r} . \tag{3}$$

Here N_a and N_r are the number of cells with attractive and repulsive magnetostatic interaction, respectively. M_S denotes the saturation magnetization. Figure 4(b) shows a local surface angle map for the same matrix. We declare the term "surface angle" as the angle between the microtube surface normal and the perpendicular z-coordinate. In this notation, the surface angle is equivalent to the former definition of ϕ since the external magnetic field points along the z-axis. Note

that the value of each pixel of the 64×16 px map in Fig. 4(b) was determined by means of a nearest neighbor approximation using the original 1024×256 px data of surface angles between the local microtube surface normal and the direction of the perpendicular magnetic field. The matrix size of 64×16 cells is a trade-off between the requirement of small cells to investigate the magnetization reversal on a length scale as small as possible and a required minimum cell size to properly calculate the local surface angle. Next we form groups of cells with each group associated with an interval of surface angles. The angle intervals are calculated in two different ways: (i) a constant number of cells, i.e., $N_a + N_r = 64$, and variable interval size; (ii) constant interval size, i.e. <5 degrees, and variable number of cells. For each angle interval the net magnetization is evaluated according to Eq. (3).

The first approach is used to analyze the demagnetized state shown in Fig. 4, and for the field-dependent measurements discussed below. Calculating the mean value of the magnetization states of all 1024 surface cells (see Fig. 4) yields a normalized net magnetization of $M/M_S = 0.094$ for the entire MFM scan area, corresponding to a nearly demagnetized microtube. At larger surface angles, however, this evaluation method considerably deviates from the anticipated demagnetized state [see Fig. 4(c)]. This discrepancy is due to methodological challenges of MFM with detecting magnetic stray fields from domains at large surface angles and will be discussed later.

The same evaluation method based on surface angle intervals with a constant number of 64 cells is employed to analyze the magnetization reversal process beginning with the saturated remanent state of the microtube (MFM maps in Fig. 3). Figure 5(a) shows the angular dependence of the normalized net magnetization for various external fields. The second evaluation method is employed to determine the switching fields for one specific fixed angle interval size, and to estimate the field dependence of the normalized net magnetization [Fig. 5(b)].

Note the synonymous use of "magnetic switching field" and "magnetic coercivity" at the local scale in the investigated perpendicularly magnetized films. The approximated states with zero net magnetization are retrieved by linear
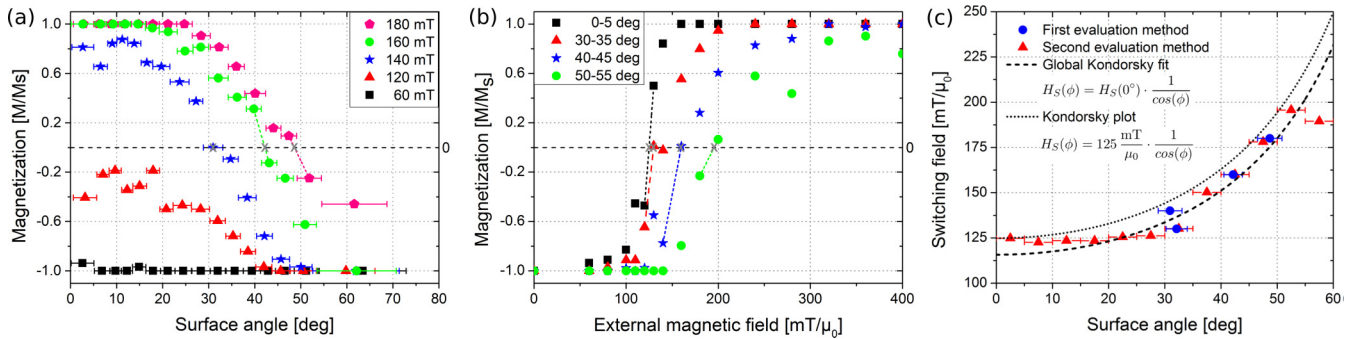
FIG. 5. (a) Normalized net magnetization according to Eq. (3), for variable size of angle intervals and fixed number of cells. It is based on the evaluation of the magnetic stray-field maps shown in Fig. 3 and their respective surface angle maps. (b) Field-dependent normalized net magnetization according to Eq. (3), for constant size of angle intervals and variable number of cells. (c) Angular dependence of the local switching field for the first (●) and second (▲) evaluation methods. The data are fitted using the global Kondorsky-type $1/\cos(\phi)$ function and a modified version based on an experimentally determined $H_S(0°) = 125 \frac{\mathrm{mT}}{\mu_0}$.

interpolation [Figs. 5(a) and 5(b)]. Hence, in the second evaluation method the field resolution is not limited to the pre-defined magnetic field steps. The occurrence of additional data points (▲) in the surface angle range 0°–30° [Fig. 5(c)] makes the second method more suited to determine the switching field at small surface angles, paying tribute to the shallow slope of the Kondorsky function at small angles.

D. Stray-field mapping at steep surfaces

The following paragraph is dedicated to challenges of MFM with detecting magnetic stray fields from domains at large surface angles. Considering the extreme case of $\phi = 90°$, a horizontally aligned cantilever oscillating in the z-direction translates to an in-plane oscillation with respect to the surface plane. In this case, the measured z-derivative of the magnetostatic force corresponds to a local in-plane MFM measurement similar to MFM in pendulum geometry [21,22]. Hence magnetic domains separated by domain walls parallel to the tip oscillation do not contribute to an MFM signal due to absent z-derivatives of the stray-field components along this direction [Fig. 6(a)]. Although the internal structure of domain walls, i.e., domain wall type, dictates the longitudinal component of the local magnetization, the latter does not directly translate to a longitudinal stray-field component. Namely, Bloch walls observed in symmetric Co/Pd multilayers [13] generate a longitudinal magnetization [10], parallel to the z-direction discussed here; Néel walls cause a perpendicular component at the expense of a longitudinal one [10]. Either wall has a normal (radial) stray-field component but lacks a longitudinal contribution for absent Bloch lines. In contrast, domain walls perpendicular to the tip oscillation [Fig. 6(b)] generate stray-field z-components with corresponding z-derivatives and emergent MFM contrast. To minimize these systematic uncertainties at large ϕ, we limited the analysis of the MFM data to surface angles $\phi < 60°$. The recently introduced bidirectional MFM approach is a promising way to circumvent such limitations in future studies [23,24]. Bidirectional MFM employing two modes of flexural cantilever vibration can be performed using conventional scanning force microscopy equipment but requires a special probe design.

IV. RESULTS AND DISCUSSION

Possible modifications to static properties of rolled-up magnetic nanomembranes with respect to their initial planar configuration include strain relaxation (reduced magnetostrictive anisotropy), curvature effects (chirality selection), topology-induced domain patterning, and radial/vertical repetition (increased saturation magnetization). Neither of those cases is valid in our study. First, the titanium film is heavily strained and relaxes upon rolling without noticeable effect on the magnetic properties of the Co/Pd multilayer stack. Second, curvature effects, such as magnetochirality and vector spin exchange, require substantially smaller radii, i.e., 50 nm, to compete with the governing scalar Heisenberg exchange interaction. This leaves the two scenarios of topology-induced domain patterning and modification to remanent state, switching field, and saturation magnetization. In a previous work, it was reported that both cases surface in tightly wound tubular nanomembranes [13]. The analysis shows that such a modification indeed requires tightly wound layers, otherwise leading to microtubes with properties very similar to their
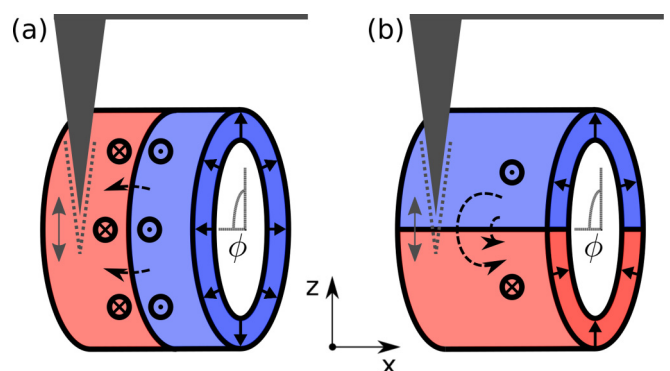

FIG. 6. Sketch of the extreme case where the MFM tip oscillates parallel to the local microtube surface ($\phi = 90°$) with two different simplified magnetic domain configurations. (a) For domain walls parallel to the tip oscillation direction, no MFM signal is expected due to vanishing magnetostatic force z-component. (b) Domain walls perpendicular to the tip oscillation direction cause a detectable MFM signal.

planar counterparts. A fully saturated remanent state after exposing to a normal magnetic field of 430 $\frac{mT}{\mu_0}$ suggests a reduced magnetostatic coupling between adjacent windings due to loosely wound nanomembrane. In fact, a comparison of the magnetization reversal process between the present microtube and a nonrolled-up planar Co/Pd multilayer film reveal values of $H_S(0° - 5°) = 125 \frac{mT}{\mu_0}$ [46] and $H_S(0°) = (127 \pm 4) \frac{mT}{\mu_0}$, respectively. This last was measured by MOKE magnetometry. The imperfect rolling up is evident in the SEM micrograph as well as in the topography scan revealing a profile with a 100-nm high step (Fig. 2) corresponding to the spacing between adjacent Co/Pd multilayer films. Fitting the Kondorsky relation to the experimental data to describe their angular dependence yields a slightly lower switching field of $H_S(0°) = (116 \pm 2) \frac{mT}{\mu_0}$ [Fig. 5(c)]. For comparison, an additional Kondorsky plot with $H_S(0°)$ fixed to the experimentally determined value of $H_S(0° - 5°) = 125 \frac{mT}{\mu_0}$ is displayed. It is obvious that the unmodified Kondorsky function with one more variable fits fairly well to experimental data. The validation to treat this angular dependence with the unmodified Kondorsky function is given by a substantially smaller switching field $H_S(0°)$ compared to the anisotropy field $H_a = 2K_u/M_S$ generated by the perpendicular magnetic anisotropy K_u in the ferromagnetic material [47]. Taking into account typical material parameters for the measured Co/Pd thin film, i.e., $K_u = 200 \, \text{kJ/m}^3$ and $M_S = 500 \, \text{kA/m}$ [48], we obtain $H_a = 800 \frac{mT}{\mu_0}$, which is more than six times larger than $H_S(0°) = 125 \frac{mT}{\mu_0}$. For $H_S(0°)$ closer to H_a, the angular dependence of the switching field deviates from the simple $1/\cos(\phi)$ relation and requires modification to the Kondorsky function [47]. This implies, in particular, that the minimal switching field $H_{S,\text{min}}$ is no longer located at $\phi = 0°$. Switching fields approaching the anisotropy field transform the Kondorsky-type character into a Stoner-Wohlfarth-like behavior (Fig. 1). For instance, H_S is minimal at 45° if $H_S(0°)$ equals H_a [47]. In the present case [Fig 5(c)], the minimal switching field is $H_{S,\text{min}} = H_S(7.5°) = 123 \frac{mT}{\mu_0}$ [49]. Together with an apparent delayed onset of the Kondorsky relation, this finding indicates a minor yet noticeable Stoner-Wohlfarth-like contribution. The governing mechanism of a pinning site dominated magnetization reversal is reflected in Fig. 3, where the switching begins in the central region of the microtube and stops at large surface angles. In these border regions, the domain walls are pinned and do not move until a larger field is applied sufficient to push the domain wall further toward regions with even higher surface angles. Note that sputtered Co/Pd or Co/Pt thin films are ferromagnetic polycrystalline materials

that are known to have large domain wall pinning that limits their application potential for spintronics applications using skyrmions. An alternative, which is from synthesis challenges equivalent, are amorphous ferrimagnetic GdCo films [10,50] that promise large domain wall and skyrmion velocities owing to low spin damping, negligible pinning at grain boundaries, and nearly compensated moments. This material may also be a good prototypical system to observe curvature driven chirality selection.

V. SUMMARY AND OUTLOOK

We spatially resolved the magnetization reversal process in radially magnetized loosely wound tubular geometries facilitating multi-frequency magnetic force microscopy. On the microscale due to absent magnetostatic interwinding coupling, the rolled-up nanomembrane behaves like a planar film with perpendicular magnetic anisotropy, whose angular dependence of the switching field can be described by the Kondorsky model. This field dependence agrees well with previous works on tightly wound microtubes using magnetic x-ray tomography. The present work is a first demonstration of multifrequency MFM as a versatile microscopy tool to investigate field-dependent magnetization processes at the nanoscale on curved surfaces with large slopes. The fundamental limitation of MFM contrast formation in case of large surface angles $\phi \approx 90°$ can be overcome utilizing advanced MFM probes and modes of operation that offer multidirectional tip oscillations. Based on its performance and potential, we envision that multifrequency MFM will emerge as a cost-efficient table-top tool with essential contributions to the study of 3D nanomagnetism, complementing high-resolution Lorentz microscopy, vector field electron tomography, and magnetic x-ray microscopy and tomography requiring large-scale user facilities.

ACKNOWLEDGMENTS

[1] A. Fernández-Pacheco, R. Streubel, O. Fruchart, R. Hertel, P. Fischer, and R. P. Cowburn, Nat. Commun. **8**, 15756 (2017).

[2] E. J. Smith, D. Makarov, S. Sanchez, V. M. Fomin, and O. G. Schmidt, Phys. Rev. Lett. **107**, 097204 (2011).

[3] R. Streubel, P. Fischer, F. Kronast, V. P. Kravchuk, D. D. Sheka, Y. Gaididei, O. G. Schmidt, and D. Makarov, J. Phys. D: Appl. Phys. **49**, 363001 (2016).

[4] Y. Gaididei, V. P. Kravchuk, and D. D. Sheka, Phys. Rev. Lett. **112**, 257203 (2014).

[5] R. Hertel, Spin **03**, 1340009 (2013).

[6] M. Yan, A. Ka'kay, S. Gliga, and R. Hertel, Phys. Rev. Lett. **104**, 057201 (2010).

[7] D. Karnaushenko, D. D. Karnaushenko, D. Makarov, S. Baunack, R. Schäfer, and O. G. Schmidt, Adv. Mater. **27**, 6582 (2015).

[8] T. Ueltzhöffer, R. Streubel, I. Koch, D. Holzinger, D. Makarov, O. G. Schmidt, and A. Ehresmann, ACS Nano **10**, 8491 (2016).

[9] S. S. P. Parkin, M. Hayashia, and L. Thomas, Science **320**, 190 (2008).

[10] R. Streubel, C.-H. Lambert, N. Kent, P. Ercius, A. T. N'Diaye, C. Ophus, S. Salahuddin, and P. Fischer, Adv. Mater. **30**, 1800199 (2018).

[11] C. Phatak, A. K. Petford-Long, and M. De Graef, Phys. Rev. Lett. **104**, 253901 (2010).

[12] T. Tanigaki, Y. Takahashi, T. Shimakura, T. Akashi, R. Tsuneta, A. Sugawara, and D. Shindo, Nano Lett. **15**, 1309 (2015).

[13] R. Streubel, F. Kronast, P. Fischer, D. Parkinson, O. G. Schmidt, and D. Makarov, Nat. Commun. **6**, 7612 (2015).

[14] C. Donnelly, M. Guizar-Sicairos, Valerio Scagnoli, S. Gliga, M. Holler, J. Raabe, and L. J. Heyderman, Nature **547**, 328 (2017).

[15] D. Sanz-Hernández, R. F. Hamans, J.-W. Liao, A. Welbourne, R. Lavrijsen, and A. Fernández-Pacheco, ACS Nano **11**, 11066 (2017).

[16] H. A. M. de Gronckel, C. H. W. Swüste, K. Kopinga, and W. J. M. de Jonge, Appl. Phys. A **49**, 467 (1989).

[17] T. Yang, F. Pan, and B. X. Liu, Phys. Stat. Sol. (a) **142**, 443 (1994).

[18] H. J. G. Draaisma, F. J. A. den Broeder, and W. J. M. de Jonge, J. Appl. Phys. **63**, 3479 (1988).

[19] J. Zarpellon, H. F. Jurca, J. Varalda, C. Deranlot, J. M. George, M. D. Martins, S. O. Parreiras, C. Müller, and D. H. Mosca, RSC Adv. **4**, 8410 (2014).

[20] J. Schwenk, X. Zhao, M. Bacani, M. A. Marioni, S. Romer, and H. J. Hug, Appl. Phys. Lett. **107**, 132407 (2015).

[21] K. Kim, Y. Seo, H. Jang, S. Chang, M.-H. Hong, and W. Jhe, Nanotechnol. **17**, 201 (2006).

[22] A. DiCarlo, M. R. Scheinfein, and R. V. Chamberlin, Appl. Phys. Lett. **61**, 2108 (1992).

[23] C. F. Reiche, S. Vock, V. Neu, L. Schultz, B. Büchner, and T. Mühl, New J. Phys. **17**, 013014 (2015).

[24] T. Mühl, J. Körner, S. Philippi, C. F. Reiche, A. Leonhardt, and B. Büchner, Appl. Phys. Lett. **101**, 112401 (2012).

[25] E. C. Stoner and E. P. Wohlfarth, Philos. Trans. R. Soc. Lond. A **240**, 599 (1948).

[26] C. Tannous and J. Gieraltowski, Eur. J. Phys. **29**, 475 (2008).

[27] A. Aharoni and S. Shtrikman, Phys. Rev. **109**, 1522 (1958).

[28] W. F. Brown, J. Appl. Phys. **30**, S62 (1959).

[29] R. Ferré, K. Ounadjela, J. M. George, L. Piraux, and S. Dubois, Phys. Rev. B **56**, 14066 (1997).

[30] N. A. Usov, A. P. Chen, A. Zhukov, and J. González, J. Appl. Phys. **104**, 083902 (2008).

[31] E. Kondorsky, Phys. Z. Sowjet. **11**, 597 (1937).

[32] E. Kondorsky, J. Phys. (Moscow) **2**, 161 (1940).

[33] W. Wernsdorfer, C. Thirion, N. Demoncy, H. Pascard, and D. Mailly, J. Magn. Magn. Mater. **242**, 132 (2002).

[34] M. Delalande, J. de Vries, L. Abelmann, and J. C. Lodder, J. Magn. Magn. Mater. **324**, 1277 (2012).

[35] A. Hubert and R. Schäfer, *Magnetic Domains: The Analysis of Magnetic Microstructures* (Springer, New York, 1998).

[36] J. M. D. Coey, *Magnetism and Magnetic Materials* (Cambridge University Press, Cambridge, England, 2010).

[37] D. Roy and P. S. A. Kumar, J. Appl. Phys. **115**, 073906 (2014).

[38] T. R. Albrecht, P. Grütter, D. Horne, and D. Rugar, J. Appl. Phys. **69**, 668 (1991).

[39] J. Lohau, S. Kirsch, A. Carl, G. Dumpich, and E. F. Wassermann, J. Appl. Phys. **86**, 3410 (1999).

[40] D. Ziegler and A. Stemmer, Nanotechnol. **22**, 075501 (2011).

[41] B. I. Kim, Rev. Sci. Instrum. **80**, 023702 (2009).

[42] R. Streubel, J. Lee, D. Makarov, M.-Y. Im, D. Karnaushenko, L. Han, R. Schäfer, P. Fischer, S.-K. Kim, and O. G. Schmidt, Adv. Mater. **26**, 316 (2014).

[43] J. Kerr, Philos. Mag. **3**, 321 (1877).

[44] I. V. Soldatov and R. Schäfer, J. Appl. Phys. **122**, 153906 (2017).

[45] W. M. Li, Y. Yang, Y. J. Chen, T. L. Huang, J. Z. Shi, and J. Ding, J. Magn. Magn. Mater. **324**, 1575 (2012).

[46] MFM measurements of a second microtube with comparable geometry yield $H_S(0° - 5°) = 129 \frac{\text{mT}}{\mu_0}$.

[47] F. Schumacher, J. Appl. Phys. **70**, 3184 (1991).

[48] R. Streubel, P. Fischer, M. Kopte, O. G. Schmidt, and D. Makarov, Appl. Phys. Lett. **107**, 112406 (2015).

[49] Both location and reduction with respect to $H_S(0°)$ are confirmed by MFM measurements of the second microtube, for which $H_{S,\min} = H_S(7.5°) = 127 \frac{\text{mT}}{\mu_0}$.

[50] L. Caretta, M. Mann, F. Büttner, K. Ueda, B. Pfau, C. M. Günther, P. Hessing, A. Churikova, C. Klose, M. Schneider, D. Engel, C. Marcus, D. Bono, K. Bagschik, S. Eisebitt, and G. S. D. Beach, Nat. Nanotechnol. **13**, 1154 (2018).